

Characterization of correlations of fast-ion H-alpha measurement volumes in Wendelstein 7-X by particle tracking

Cite as: Rev. Sci. Instrum. **93**, 123503 (2022); <https://doi.org/10.1063/5.0128594>

Submitted: 29 September 2022 • Accepted: 11 November 2022 • Published Online: 02 December 2022

 Jacob Emil Mencke,  Dmitry Moseev, Mirko Salewski, et al.



View Online



Export Citation



CrossMark

ARTICLES YOU MAY BE INTERESTED IN

[Gas puff imaging on the TCV tokamak](#)

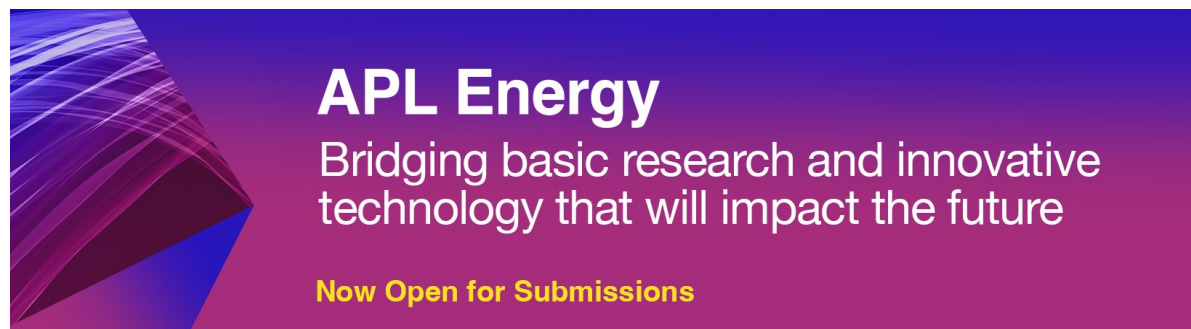
Review of Scientific Instruments **93**, 123504 (2022); <https://doi.org/10.1063/5.0126398>

[Conceptual design of a heavy ion beam probe diagnostic for the Wendelstein 7-X Stellarator](#)

Review of Scientific Instruments **93**, 113309 (2022); <https://doi.org/10.1063/5.0101788>

[Performance improvement of space-resolved extreme ultraviolet spectrometer by use of complementary metal-oxide semiconductor detectors at the Experimental Advanced Superconducting Tokamak](#)

Review of Scientific Instruments **93**, 123501 (2022); <https://doi.org/10.1063/5.0104225>



APL Energy
Bridging basic research and innovative
technology that will impact the future
Now Open for Submissions

Characterization of correlations of fast-ion H-alpha measurement volumes in Wendelstein 7-X by particle tracking

Cite as: Rev. Sci. Instrum. 93, 123503 (2022); doi: 10.1063/5.0128594

Submitted: 29 September 2022 • Accepted: 11 November 2022 •

Published Online: 2 December 2022



View Online



Export Citation



CrossMark

Jacob Emil Mencke,^{1,2,a)} Dmitry Moseev,³ Mirko Salewski,¹ Mads Rud Larsen,¹
Bo Simmendefeldt Schmidt,¹ Henrik Järleblad,¹ Samuel Lazerson,³ Peter Zsolt Poloskei,³
Oliver Ford,³ and Wendelstein 7-X Team^{b)}

AFFILIATIONS

¹Department of Physics, Technical University of Denmark, Fysikvej, 2800 Kgs. Lyngby, Denmark

²Swiss Plasma Center (SPC), Ecole Polytechnique Fédérale de Lausanne (EPFL), CH-1015 Lausanne, Switzerland

³Max-Planck-Institut fuer Plasmaphysik, Wendelsteinstraße 1, 17491 Greifswald, Germany

^{a)}Author to whom correspondence should be addressed: jacob.mencke@epfl.ch

^{b)}See Thomas Sunn Pedersen et al., Nucl. Fusion **62**, 042022 (2020) for the full list of W7-X team members.

ABSTRACT

This paper characterizes the correlation of simultaneous measurements with different fast-ion H-alpha (FIDA) spectroscopy sightlines on Wendelstein 7-X. Using a collisionless guiding-center code, it is shown that, for two investigated volumes in the bulk of the plasma, some regions of phase space are correlated and the magnetic configuration has little influence on this correlation. For the sightlines of the FIDA system, the correlation between these is explained well by the magnetic configuration. Sightlines with measurement volumes at the same spatial locations have the highest correlation, and sightlines with measurement volumes near the same flux surface but on different sides of the magnetic axis have a high correlation. The correlation between the blueshifted signal in the starting sightline and redshifted signal in the detection sightline is investigated, demonstrating that it is possible to investigate any finite interval of detection wavelengths. Due to the different shapes of the weight functions for the toroidal and oblique sightlines, the blue-redshift correlation is very different from the total-spectrum correlation. The correlation between the toroidal and oblique sightline fans is relatively much larger than the internal correlation in the oblique sightlines, which is however, much larger than the internal correlation in the toroidal sightlines. This is a result of the dependence of the weight functions on the angle between the sightline and magnetic field, illustrating how important it is for the FIDA sightlines to cover different angles with the magnetic field.

© 2022 Author(s). All article content, except where otherwise noted, is licensed under a Creative Commons Attribution (CC BY) license (<http://creativecommons.org/licenses/by/4.0/>). <https://doi.org/10.1063/5.0128594>

I. INTRODUCTION

It is important to measure the fast-ion phase-space distribution function in tokamaks and stellarators, since it tells us much about the fast-ion confinement and the drive or damping of instabilities in the plasma.¹ In a toroidally symmetric tokamak, the phase-space distribution function can be parameterized in three coordinates, for example, the energy, the maximum major radius of an orbit, and the pitch, $p = v_{\parallel}/v$, at the maximum major radius.² However, real tokamaks are not toroidally symmetric, since the magnetic coil systems consist of 10–20 individual toroidal field coils rather than a tightly

wound solenoid, leading to magnetic-field ripples.³ If we do not assume toroidal symmetry in position space, the toroidal canonical angular momentum is not a constant of motion, and the phase-space distribution function does not reduce to 3D. Due to the fast gyration of the ions, the velocity distribution functions can be described in 2D, e.g., using the parallel and perpendicular velocities with respect to the magnetic field, $(v_{\parallel}, v_{\perp})$, as coordinates. Stellarators possess an inherent toroidal asymmetry, implying that the real-space part of the phase-space distribution function must be three dimensional. Subsequently the phase space distribution function must be 5D. In order to understand the state of the plasma eventually, it is a goal

to reconstruct these distribution functions in 5D.⁴ Such reconstructions are nowadays possible in the 2D velocity space at a single point in position space^{5–15} and in symmetric tokamaks in 3D,² but they are extremely difficult in 5D, since the number of sightlines is restricted by the limited space around the machine and the limited optical access to the machine. To have any chance of reconstructing a 5D velocity distribution function from measurements, we must place the diagnostics strategically, so that they deliver complementary information. Here, we present an analysis of the correlation between the sightlines of the fast-ion H-alpha (FIDA) spectroscopy at Wendelstein 7-X (W7-X). The acronym FIDA is used in light of the future application of the system where deuterium plasmas will be investigated using the D-alpha line. For integrated data analysis of fast-ion measurements, we view the set of available diagnostics as a single diagnostic, allowing us to apply tomographic inversion. For this endeavor, knowledge of correlation between different measurements provides valuable prior information. The use of prior information is essential for 5D inference, since the 5D parameter space is so vast, and we never have enough diagnostic data to perform inversions without prior information. To date, W7-X has operated with hydrogen-1, and, hence, we use hydrogen-1 in our computations. This isotope will simply be referred to as hydrogen throughout this paper.

Neutral beam injection (NBI) is often used for heating plasmas during discharges on W7-X. The particles stemming from this beam will form a 5D slowing-down distribution function in magnetohydrodynamically quiescent plasmas with no anomalous transport.^{14,15} These functions are of immense importance, in order to understand the state and development of the plasma. Since the ions from NBI are born with specific energies and pitches, the fast-ion velocity distribution function is highly non-Maxwellian. The pitch is defined as the parallel velocity divided by the speed, $p = v_{\parallel}/v$. The form of the distribution function is required in order to calculate whether the fast ions drive the MHD modes unstable, which leads to anomalous fast-ion transport. It may also be possible to suppress turbulence.¹⁶

Fast-ion diagnostics often rely on measuring Doppler-shifted waves, providing clues about the fast-ion velocity distribution function.^{2,5,17} This principle is especially clear for charge-exchange recombination spectroscopy (CXRS), which detects emitted photons from a charge-exchange reaction.^{18–20} Two other examples are collective Thomson scattering, where electromagnetic waves with wavelengths in the millimeter scale are injected and the wavelengths of the scattered waves are measured,^{21–24} and gamma-ray spectroscopy.^{13,25–27}

A special type of CXRS is FIDA spectroscopy, which detects the change in wavelength from a fast deuterium or hydrogen atom undergoing charge exchange and emitting a Balmer alpha photon.^{1,18,19,28} This method is particularly well suited for characterizing and measuring the NBI slowing-down distribution function, since the sensitivity of FIDA is largest in the energy range typical for NBIs. Spectrometers similar to the ITER are installed at W7-X, which detects photons in three branches, out of which one is centered around the Balmer alpha line. This system is already used to measure the beam density and electron and ion temperature and density.¹⁸ Moreover, it could also be used to characterize the beam deposition profile or infer the fast-ion distribution

function. FIDA is installed and successfully used on many tokamaks and stellarators.^{29–38}

As a first step toward getting the 5D slowing-down distribution function using tomographic inversion, this paper will focus on characterizing the FIDA spectroscopy system of W7-X and will study the correlation among the different detectors, when the entire system is viewed, with a focus on integrated data analysis by tomographic inversion. This work will aid in identifying any weakly diagnosed regions in the phase space. The limited optical access to the plasma makes it necessary to know which existing diagnostics to use for a certain discharge in a magnetic confinement device when studying fast-ion distribution functions. Furthermore, it is valuable knowledge, which regions of phase space are well covered by the existing FIDA diagnostics. Therefore, this study comes timely in light of the upcoming campaign at W7-X, where the partially newly commissioned FIDA diagnostics will be used much more extensively than in the previous campaigns. For a full 5D fast-ion distribution function, it is practically impossible to cover the entire phase space with measurement volumes. Therefore, it is necessary to place the newly designed diagnostics strategically, such that maximum coverage of the phase space is achieved. Therefore, this study will reveal which regions of phase space are well covered by the existing FIDA diagnostics and, thus, help in proposing which regions of the phase space should be covered by the newly designed diagnostics, in order to maximize the detection of fast ions. For this paper, the analysis is done for the FIDA diagnostic at Wendelstein 7-X, but the method is much more general and can be applied for any fast-ion diagnostic in any magnetic confinement device.

This paper is structured in the following way. An introduction to the FIDA measurement system is given in Sec. II. Section III presents the method used for the correlation analysis, using two arbitrarily chosen volumes. In Sec. IV, the correlation between the different sightlines of the FIDA measurement system at W7-X is quantified. Finally, Sec. V concludes the paper.

II. THE FIDA MEASUREMENT SYSTEM OF W7-X

For further reference, the FIDA diagnostic system of W7-X is introduced, along with the weight functions of the different sightlines.¹⁸ Any diagnostic measurement, $m \in [m_1, m_2]$, with signal, s , can be seen as a convolution of the weight function, w , of the given diagnostic system, with the distribution function, f ,^{13,32}

$$s(m_1, m_2, \phi) = \int_{\text{vol}} \int_0^{\infty} \int_{-\infty}^{\infty} w(m_1, m_2, \phi, v_{\parallel}, v_{\perp}, \mathbf{x}) \times f(v_{\parallel}, v_{\perp}, \mathbf{x}) dv_{\parallel} dv_{\perp} d\mathbf{x}, \quad (1)$$

where ϕ is the angle between the diagnostic sightline and the magnetic field. It is effective splitting each weight function the following way:

$$w(m_1, m_2, \phi, v_{\parallel}, v_{\perp}, \mathbf{x}) = R(\phi, v_{\parallel}, v_{\perp}, \mathbf{x}) \text{prob}(m_1 < m < m_2 | \phi, v_{\parallel}, v_{\perp}, \mathbf{x}), \quad (2)$$

where $R(\phi, v_{\parallel}, v_{\perp}, \mathbf{x})$ is the total intensity per unit ion density and $\text{prob}(m_1 < m < m_2 | \phi, v_{\parallel}, v_{\perp}, \mathbf{x})$ is the probability of measuring $m \in [m_1, m_2]$, given a combination of $\phi, v_{\parallel}, v_{\perp}, \mathbf{x}$.¹⁹ An example of a

FIDA spectrum is shown in Ref. 1, Fig. 3. Weight functions containing the most important physics of the FIDA process can be calculated with the FIDASIM code.³⁹ However, for the purpose of our study, we will focus on the Doppler shift and neglect other physics, since the Doppler shift is most essential for the spectrum formation.

In the case of FIDA, the change in the wavelength, $\Delta\lambda$, from the wavelength in the rest frame of the emitter, λ_0 , is measured. The wavelengths of the emission lines are $\lambda_{0,D_\alpha} = 656.1$ nm and $\lambda_{0,H_\alpha} = 656.5$ nm in the frame of the emitting atom. This change in wavelength stems mainly from the Doppler shift, but also has a contribution due to the Stark effect.^{1,18–20} Neglecting the Stark effect, the probability of detecting a photon stemming from a projected velocity in the range $u \in [u_1, u_2]$ can be written as¹⁹

$$\text{prob}(u_1 < u < u_2 | \phi, v_{\parallel}, v_{\perp}) = \frac{1}{\pi} \left(\arccos \frac{u_1 - v_{\parallel} \cos \phi}{v_{\perp} \sin \phi} - \arccos \frac{u_2 - v_{\parallel} \cos \phi}{v_{\perp} \sin \phi} \right), \quad (3)$$

which depends implicitly only on the position through ϕ . The projected velocity, u , can be expressed in terms of the particle velocity and the gyro-angle γ as

$$u = v_{\parallel} \cos \phi + v_{\perp} \sin \phi \cos \gamma, \quad (4)$$

where γ is treated as a random variable, due to the large cyclotron frequency of the particles.

The Doppler shift up to approximately $\Delta\lambda \sim 2$ nm at W7-X is dominated by the bulk ions. The Doppler shift above $\Delta\lambda \sim 5$ nm is dominated by noise, while the spectrometer is unable to measure a photon with a Doppler shift above $\Delta\lambda \sim 7$ nm. When neglecting both the Stark splitting, the measurable projected velocities are in the interval given by

$$|u| \in [u_{\min}, u_{\max}], \quad (5)$$

$$u_{\min} = c \frac{\Delta\lambda_{\min}}{\lambda_0} \sim 9.14 \cdot 10^5 \frac{\text{m}}{\text{s}}, \quad (6)$$

$$u_{\max} = c \frac{\Delta\lambda_{\max}}{\lambda_0} \sim 2.28 (3.20) \cdot 10^6 \frac{\text{m}}{\text{s}}, \quad (7)$$

where the two different upper limits are indicated as $\Delta\lambda \sim 5$ (7) nm. u can have either sign. A positive u is detected with a blueshifted light, while a negative u is detected with a redshifted light. The maximum possible velocity for an NBI with hydrogen and an injection energy of 55 keV is $v_{\max} = 3.25 \times 10^6$ m/s, but due to the geometry of the NBI and the FIDA sightlines, the maximum possible projected velocities are lower than that.

The spectrometer has a temporal resolution of the order of $\delta t \sim 1$ ms and a spectral resolution of the order of $\delta\lambda \sim 0.042$ nm,^{18,20} so the projected velocity resolution is

$$\delta u = c \frac{\delta\lambda}{\lambda_0} \sim 19.18 \cdot 10^3 \frac{\text{m}}{\text{s}}, \quad (8)$$

$$N_u = 2 \frac{u_{\max} - u_{\min}}{\delta u} \sim 142 (238), \quad (9)$$

where N_u is the number of distinguishable projected-velocity measurements, remembering that both positive and negative values of u are allowed.

The FIDA system at W7-X could consist of three different fans, with a possibility of 237 sightlines in total, even though not all FIDA views are currently installed. The geometry is illustrated in Fig. 1(b). Each sightline intersects either NBI S7 or NBI S8, or both. The A21 (blue) fan views toroidally and has 4 different internal fans. A21A and A21B are parallel to each other and cover the entire path of the NBI through the plasma. A21X1 and A21X2 measure off axis with respect to the NBI's axis, such that the sightline fan is perpendicular to A21A and A21B. The M21 (green) fan crosses the NBIs at an angle of $\sim 45^\circ$. M21S7 is centered at NBI S7 and M21S8 is centered at NBI S8. There are also M21X1 and M21X2 for off-axis measurement. Finally, the T21 (yellow) fan only has one internal fan and 20 sightlines in total.¹⁸ The properties for each fan are shown in Table I, and the positioning of the measurement volumes is illustrated in Fig. 2. It is seen that the A-fans have very different angles with the magnetic field, ϕ , compared to the M- and T-fans. We refer to the sightlines in the A-fans as toroidal views and the sightlines in the M- and T-fans as oblique views. Furthermore, the spatial region of the bulk is well covered from an effective minor radius of $\rho/a \sim 0.1$.

The measurement volumes are modeled as cylinders with radius $\rho_{\text{LOS}} = 1$ cm and length given by $L_{\text{LOS}} = 10 \text{ cm}/\sin \theta$, where θ is the angle between the NBI beam path and the FIDA sightline. The radius of the NBI is assumed to be constant, $\rho_{\text{NBI}} = 5$ cm. Figure 2 illustrates the geometry. The center of each measurement volume is at the point of closest distance between the sightline and the central axis of the NBI for each FIDA sightline.

III. CORRELATION ANALYSIS BY GUIDING-CENTER TRAJECTORY CALCULATIONS

The method used in order to calculate the correlation between the FIDA measurement volumes is introduced in this section using arbitrarily chosen volumes in W7-X. The same volumes will be used when the sensitivity of the analysis to the magnetic configuration is tested at the end of Sec. IV.

For this entire paper, the simulations are done using a guiding-center simulator, BEAMS3D.^{40,41} The standard magnetic configuration referred to is EIM and for all simulations, typical values of the radial electric field ~ 3 kV/m, background ion density $\sim 5 \cdot 10^{19} \text{ m}^{-3}$, and background electron and ion temperatures ~ 2 keV are used. The background plasma and the fast ions consist of hydrogen.

First, two arbitrary volumes in the standard magnetic configuration are investigated. 10 000 particles are generated, with the pitch being linearly distributed, $p \in [p_-, p_+]$, with 100 steps and with the energy being linearly distributed, $E \in [E_{\min}, E_{\max}]$, with 100 steps, such that each particle has a unique combination of E, p . Each particle is then randomly placed in a volume, V_1 , defined by

$$(R, \psi, z) \in ([R_0 \pm \delta R/2], [\psi_0 \pm \delta\psi/2], [z_0 \pm \delta z/2]), \quad (10)$$

in ordinary cylindrical coordinates. The extent of the box is chosen such that $\delta z = \delta R = R_0 \delta\psi = 0.1$ m. A collisionless simulation is run for 150 μs , and the particles entering volume V_2 are detected. V_2 is defined equivalent to V_1 , but with different R_0, ψ_0 , and z_0 . For V_1 , $R_0 = 5.8$ m, $z_0 = 0$ m, and $\psi_0 = 0$, while for V_2 , $R_0 = 5.752$ m, $z_0 = 0.3$ m, and $\psi_0 = 72^\circ$. Figure 3 shows the almost-uniform initial

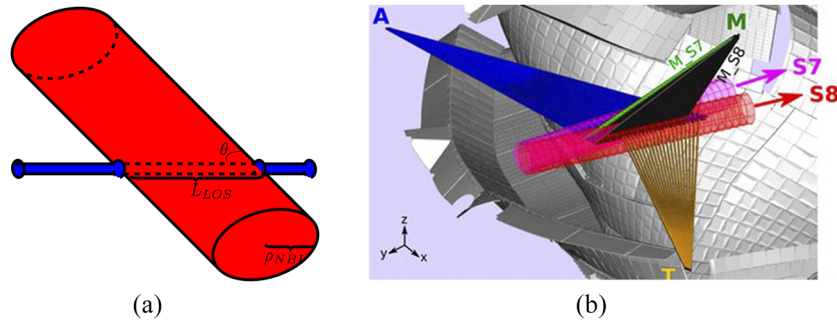


FIG. 1. (a) Sketch of the intersection between a sightline for the FIDA diagnostics in blue and the NBI injection volume in red. (b) A sketch of the actual FIDA sightlines of W7-X. It clearly shows the FIDA sightlines as fans, which only intersect the NBI S7 and NBI S8 sources. Subfigure (b) is reprinted from Ford *et al.*, Charge exchange recombination spectroscopy at Wendelstein 7-X, Rev. Sci. Instrum. **91**, 023507 (2020), with the permission of AIP Publishing.

pitch-energy particle distribution in V_1 , along with the pitch-energy particle distribution of the particles entering V_2 . The deviation from a completely uniform initial distribution is due to the slightly inaccurately calculated initial conditions. BEAMS3D uses the magnetic moment, μ , and parallel velocity, v_{\parallel} , as input velocity parameters. Thus the magnetic field strength is used to do the conversion $(E, p) \rightarrow (v_{\parallel}, \mu)$. For this conversion, the average magnetic field in the volume was used instead of the local magnetic field strength of each particle, leading to insignificant errors, due to small variations inside the volume. It is seen that only ions in certain parts of the phase space are detected in both volumes, whereas the other particles from the first volume move elsewhere.

Next, the region in the phase space in V_1 , where the particles are also observed in V_2 , is densely populated, with 10 000 particles, in order to improve statistics. A similar simulation as before is run. The initial distribution in V_1 and final distribution in V_2 are shown in Fig. 4. It is seen that the pitch-energy region detected in V_2 is similar to that started in V_1 . However, due to the finite size of each volume, not all particles in the correlated region of the phase space are actually detected in V_2 .

TABLE I. The range of angles with the magnetic field, ϕ , minimum effective minor radius, ρ/a , and number of sightlines (lines of sight) for each fan, N_{LOS} , for the different fans. $\rho/a = \infty$ means that the position is outside the last closed flux surface. The central toroidal angle, ψ_0 , is between 88–89° for all measurement volumes and the lengths, L , are between 10.0 and 12.5 cm.

Name	ϕ -range (°)	ρ/a -range	N_{LOS}
AA	2.7–9.6	0.1– ∞	40
AB	2.2–9.2	0.09– ∞	40
AX1	4.8–11.0	0.75–0.79	6
AX2	2.2–10.9	0.07–0.22	6
MS7	128.2–137.9	0.05– ∞	54
MS8	121.8–133.4	0.10– ∞	54
MX1	128.1–141.6	0.70–0.87	8
MX2	122.6–139.0	0.04–0.17	9
T	113.5–141.5	0.07–0.67	20

IV. CORRELATION BETWEEN FIDA MEASUREMENT VOLUMES

Investigating the correlation between the FIDA sightlines will give insight into the most important sightlines and help propose

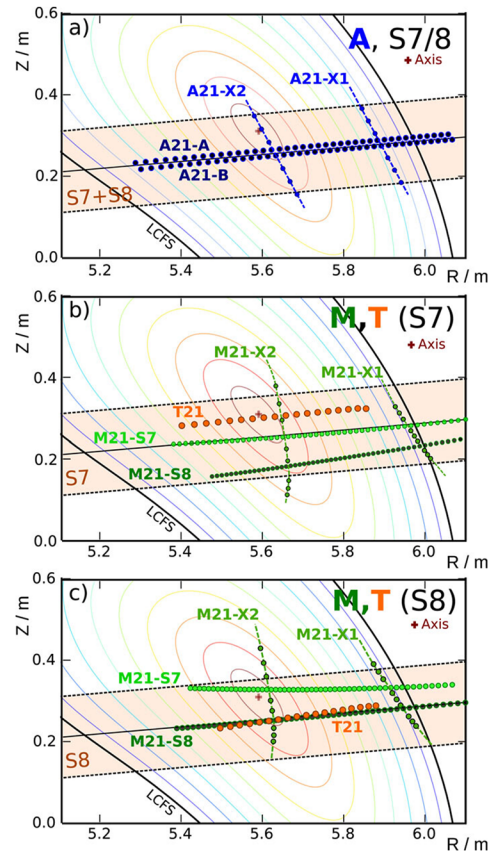


FIG. 2. RZ-view of the measurement volume of each sightline. Reprinted from Ford *et al.*, Charge exchange recombination spectroscopy at Wendelstein 7-X, Rev. Sci. Instrum. **91**, 023507 (2020), with the permission of AIP Publishing.

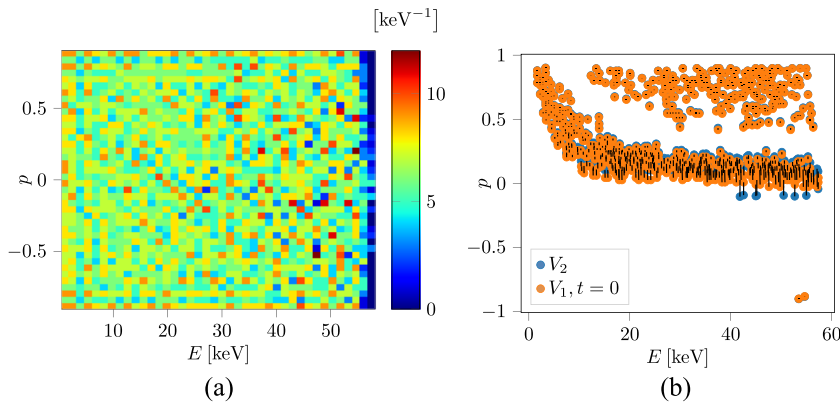


FIG. 3. (a) Starting, almost-evenly spaced, pitch-energy distribution, $p \in [-0.9, 0.9]$, $E \in [E_{\max}/100, E_{\max}]$, $E_{\max} = 55$ keV, for 10 000 particles spatially randomly distributed in V_1 . (b) Pitch-energy distribution for the particle entering volume V_2 in V_2 (blue dots) and in V_1 (orange dots).

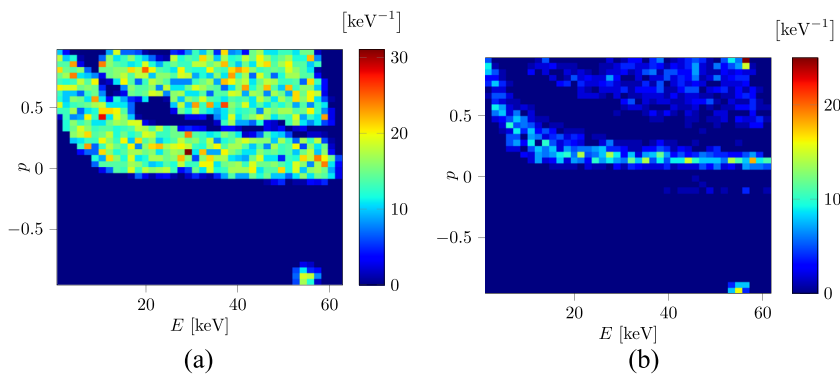


FIG. 4. (a) Starting pitch-energy distribution for 10 000 particles in V_1 , defined similarly as in Fig. 3(b) Pitch-energy distribution for the particles entering volume V_2 .

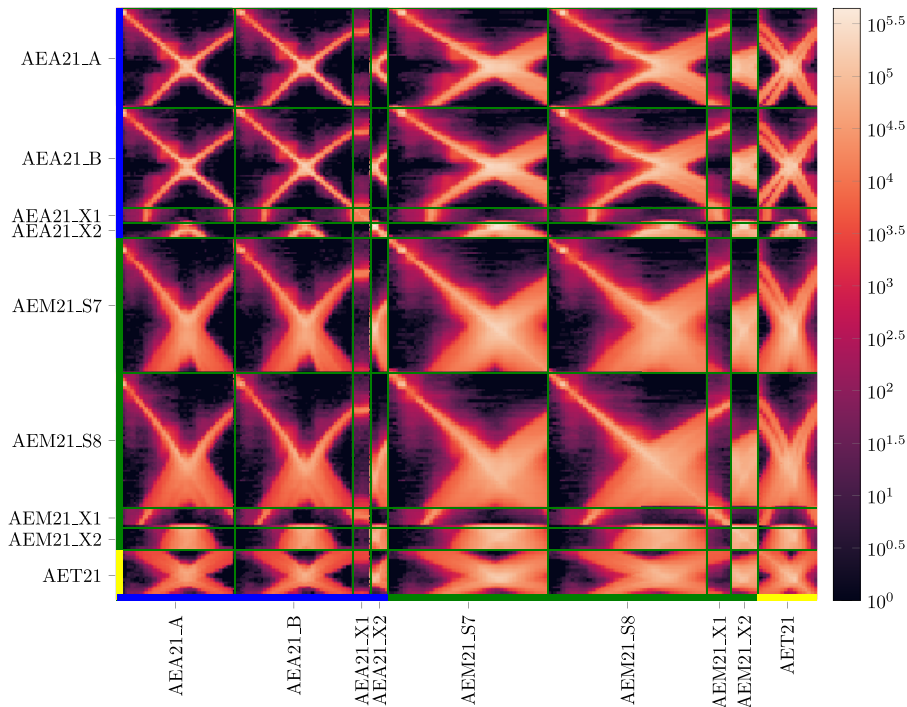


FIG. 5. Number of particles detected in the sightline at the bottom and started in the sightline at the left, plus 1 in the log10 scale. (The 1 is added to avoid infinity.) The green lines indicate a change in the FIDA fan. Each pixel corresponds to a specific fan–fan correlation. The color bar at the left and at the bottom of the figure uses the same color code as Fig. 1(b) and indicates the fan of the sightline.

which and where new diagnostics should be installed, in order to get maximum possible new information from the additional diagnostics. As before, for each sightline, a grid using energy and pitch is created with 100 points in both directions, with the pitch going from -0.9 to 0.9 and energy going from 10 to 55 keV. Each particle is placed randomly inside the given measurement volume (as defined in Fig. 1) and is tracked in a collisionless simulation for 1.5 ms, such that the entire orbit is traced out. The simulation time is ~ 10 times the collision time. Even though it might seem unjustified to do a collisionless simulation for so long a time, we take this time limit, since the collisions tend to displace particles from one orbit to another.

Since the correlation between the different sightlines is sought, at first the number of particles started in each sightline and detected in another is extracted and plotted in Fig. 5. Note the log10 scale. For each fan along the beam direction, a correlation on the top left and bottom right of the diagonal is clearly observed. This reflects the tendency of fast ions to return to the same volume in well-confined plasma. Hence, most particles return to the measurement volume from which they were started. A second highly correlated set of detectors appears in a characteristic line going from the bottom left to the top right, but not exactly on the diagonal. This highly correlated region corresponds to detection in measurement volumes near the same flux surface as the particle was started on, but on the other side of the magnetic axis. This correlation is a little lower than detection in the same volume, but substantially higher than that for volumes on flux surfaces far away. The strongest correlation is seen at the intersection of the diagonal from the top left to the bottom right and the oblique line from the bottom left to the top right. This is a result of the magnetic configuration with nested flux surfaces. In the center, the flux surfaces are more slender; so, the particles on

these pass a given measurement volume more often. Moving outward, the flux surfaces become larger, and, therefore, the count of detected particles becomes lower.

This first step of the correlation analysis reveals which particles appear in any pair of measurement volumes. In FIDA measurements, particles are detected in particular wavelength ranges, according to their velocities projected onto the sightlines. We can, therefore, extend our analysis to consider detection in particular wavelength ranges in both detectors. The presence of thermal features always makes the wavelength range around the H-alpha line unusable for fast-ion diagnostic. Excluding the wavelength range of the thermal feature in FIDA spectra, each detected particle started in the measuring volume of FIDA sightline j and detected in k is weighted by the weight

$$w_{jk} = \sum_{\text{par}_{jk}} S_{k, \text{par}} S_{j, \text{par}}, \quad (11)$$

$$S_{i, \text{par}} = \begin{cases} \frac{1}{\pi} \left[\arccos \left(\frac{u_{\min} - v_{\parallel, \text{par}} \cos \phi_i}{v_{\perp, \text{par}} \sin \phi_i} \right) \right. \\ - \arccos \left(\frac{u_{\max} - v_{\parallel, \text{par}} \cos \phi_i}{v_{\perp, \text{par}} \sin \phi_i} \right) \\ + \arccos \left(\frac{-u_{\max} - v_{\parallel, \text{par}} \cos \phi_i}{v_{\perp, \text{par}} \sin \phi_i} \right) \\ \left. - \arccos \left(\frac{-u_{\min} - v_{\parallel, \text{par}} \cos \phi_i}{v_{\perp, \text{par}} \sin \phi_i} \right) \right] \end{cases}, \quad (12)$$

where the sum is over all particles started in j and detected in k . Using this weight, we select particles with significant Doppler shifts

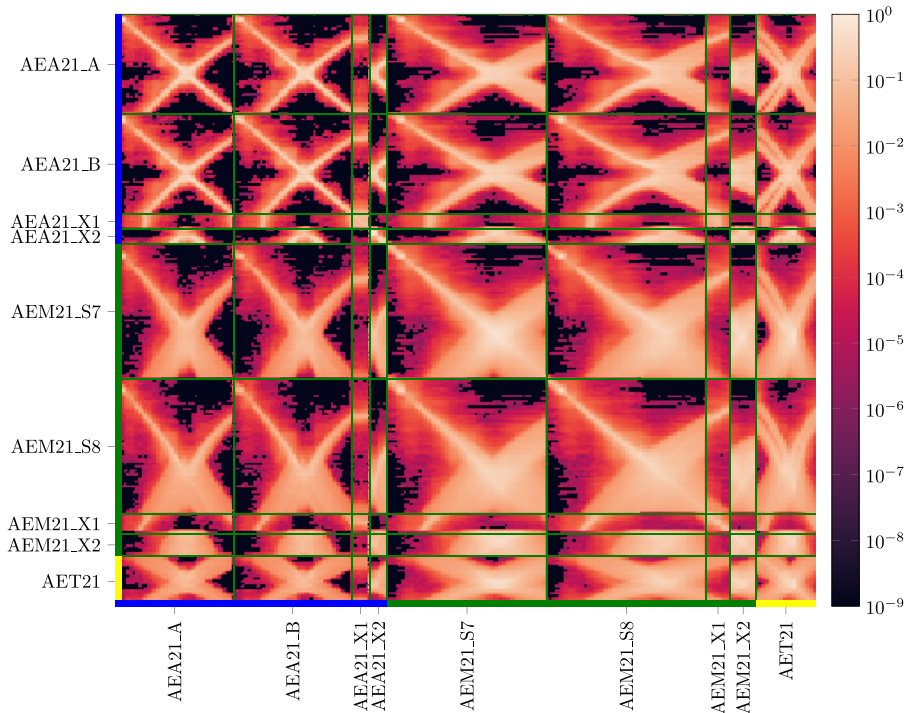


FIG. 6. Probabilities of a detection, given an emission for the LOS of W7-X. (a) and (c) for the toroidal (blue) fans. $\phi \sim 9.4^\circ$. (b) and (d) for the oblique (green or yellow) fans. $\phi \sim 136^\circ$. (a) and (b) the entire spectrum (red and blueshifted parts). (c) and (d) only the blueshifted spectrum.

in both detectors. Figure 6 shows typical weight functions, $s_{i,\text{par}}$, for the sightlines. For the blueshifted spectrum, only the first two terms of $s_{i,\text{par}}$ are used. Be aware that the blueshifted part of the spectrum $u > 0$ is identical to the redshifted part $u < 0$, if it is mirrored around $p = 0$. Note that the same method can be used to account for parts of the FIDA spectra polluted by impurity lines or direct beam emission. $s_{i,\text{par}}$ is the probability of detecting a photon emitted by particle par in measurement volume i . The probability of a particle emitting a photon is neglected altogether. As a first approximation, the probability that a photon is emitted is proportional to the time spent inside the measurement volume, but since there are dominant effects, such as the neutral density,^{1,19,32} this probability is neglected.

Since the measurement volumes are small, it is assumed that the magnetic field direction is constant, and so is the angle with the magnetic field ϕ_i . The first two terms of Eq. (12) correspond to the probability of detecting a blueshifted photon and the last two, to the probability of detecting a redshifted photon. This corresponds to a measurement where the distribution function is a sum over delta functions in E , p , and \mathbf{x} ,

$$f_{jk}(p, E, \mathbf{x}) = \sum_{\text{par}_{jk}} \delta(p - p_{\text{par}}) \delta(E - E_{\text{par}}) \delta(\mathbf{x} - \mathbf{x}_{\text{par}}), \quad (13)$$

where the equivalent of Eq. (1) in the (E, p) space is used. The correlation between the measurement volumes only for particles with significant Doppler shifts is shown in Fig. 7. In Fig. 7, all particles with small projected velocities, $|u| < 9.14 \cdot 10^5$ m/s, are removed. These particles also tend to have small drift velocities, which means that they tend to stay close to the flux surface. Note that the fast ions moving perpendicular to the sightlines have no Doppler shifts but substantial drift velocities. Nevertheless, a larger fraction of low-energy fast ions is deselected compared to high-energy ions. Removing these particles decreases the particle count close to the

diagonal and the oblique line from the bottom left to the top right. The elements far away from these lines always require large drift velocities and, therefore, attain larger weights relative to these lines. Since for passing particles, the accumulated drift over an entire orbit vanishes,⁴² the correlation off the bright diagonal and oblique line comes from the trapped particles. Since these regions observe a relatively smaller decrease in correlation when taking the weight function into account, it is easier to detect the trapped particles compared to the passing. Figures 5 and 7 are both fairly symmetric about the diagonal, from the top left to the bottom right. The counts of particles started and detected in measurement volume A and detected in B are about the same as the counts of particles started and detected in B and detected in A . This is most likely due to the time-inversion symmetry of the collisionless simulations and the fact that the FIDA weight function is symmetric when only taking the Doppler shift into account and using the red-shifted and blue-shifted wings. Since each particle in the simulation has a partner with the same pitch magnitude, opposite sign, and the same energy in each measurement volume, if a particle moves from measurement volume A to B , changing its pitch and energy from (p_A, E_A) to (p_B, E_B) , the particle started in B with $(-p_B, E_B)$ will move to A and end up with the pitch and energy $(-p_A, E_A)$. This is further explained by conservation of energy and the adiabatic invariance of the magnetic moment of particles and the fact that the magnetic field strength and electric potential are similar across all sightlines near the same flux surfaces, such that the weight function, energy, and pitch will be similar each time a particle is detected in a given sightline.

It is, in principle, possible to do a similar analysis, replacing $s_{k,\text{par}}$ or $s_{j,\text{par}}$ with the probability of a detection, given an emission for any projected velocity interval. That way, it is possible to go down to the smallest detectable u -interval, which shows the probability of a detection in a small interval around u_k in the first

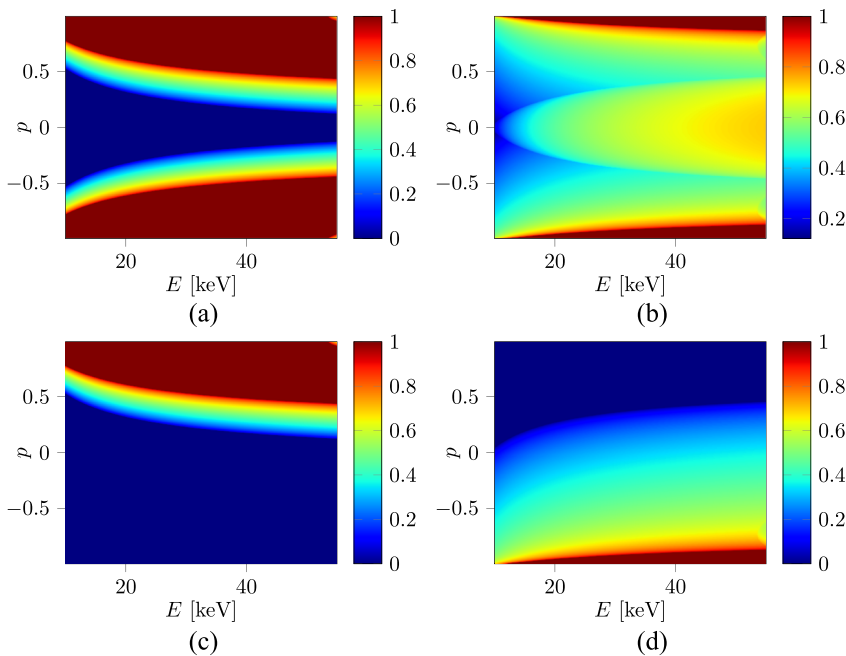


FIG. 7. Weighted total signal in the sightline at the bottom for the distribution function started in the sightline at left, normalized against the maximal value, 93 120, plus 10^{-9} in the log 10 scale. The weight is the probability of detecting a photon, given an emission in the detection and starting sightline.

volume and in a small interval around u_j in the second volume. This will show how the sightlines can complement each other, such that the combined information might lead to an inference of the particle velocities. Rather than attempting a full analysis here, we illustrate the insights gained by studying two broad velocity bins: One bin contains all particles that are detected on the blue-shifted side, and the other, red-shifted. This could be arbitrarily refined down to the spectral resolution of the instrument. The first two terms of Eq. (12) correspond to a detection in the blueshifted part of the spectrum and the last two terms correspond to a detection in the redshifted part of the spectrum. An example of the correlation between blueshifted detections in the starting volume and redshifted detections in the detection volume is shown in Fig. 8. Due to the different angles to the magnetic field for the toroidal (blue) and oblique (green or yellow) fans, the internal correlation in the toroidal or oblique fans decreases relative to the cross correlation between these fans. This is because the toroidal fans have a small angle to the magnetic field, $\phi_{\text{tor}} \sim 10^\circ$, and the oblique fans have a large angle to the magnetic field, $\phi_{\text{obl}} \sim 135^\circ$. Since the $\phi_{\text{tor}} < 90$ deg and $\phi_{\text{obl}} > 90$ deg, highly passing particles, $1 \gtrsim |p| \gg 0$ detected blueshifted in the toroidal fans will be detected redshifted in the oblique fans and vice versa. Furthermore, since for the oblique fans $180^\circ - \phi_{\text{obl}} \sim 45^\circ$, the projected velocity has a significant component perpendicular to the magnetic field. Therefore, these sightlines are able to detect particles with smaller pitch. This also becomes evident from Fig. 6. Recall that the measurements of particles with small projected velocities are dominated by the bulk ions and, therefore, useless in the reconstruction of the fast-ion distribution function. This means that the oblique fans can detect energetic particles with

much smaller pitch and are even able to detect photons from energetic particles with either sign of pitch. For the same reason, a particle with given pitch has a non-zero probability to be detected on the blue-shifted side in one volume and on the red-shifted side in another volume in the oblique fan. Therefore, a much higher internal correlation among the oblique fans is observed. Note that the oblique fans can detect trapped particles with pitches close to zero.

A similar analysis as in Sec. III is done for the low iota (DBM), high iota (FTM), low mirror (AIM), and high mirror (KJM) magnetic configurations. The simulation with a densely populated region of interest is shown here, to illustrate how little an effect the magnetic configuration has on the correlation between the phase space of the two regions in question (V_1 and V_2). The difference between the detected particles in V_2 relative to the standard magnetic configuration is shown in Fig. 9. It is seen that the relative difference is below 2%, which is attributed to numeric noise. Therefore, it is reasonable to assume that the orbit analysis for the standard configuration is applicable for other magnetic configurations on W7-X. However, the two volumes are volumes with identical magnetic configurations, since the W7-X has a 5-fold symmetry such that the magnetic configuration repeats after moving 72° toroidally. Thus, changes in pitch due to a relative change in the magnetic field strength for the two volumes are not observed. For analysis specific to a particular discharge, the correct magnetic equilibrium should be used. Although the magnetic confinement is important in assessing the fast-ion confinement properties, the effect of different magnetic configurations on the correlation between different volumes does not appear to be large.

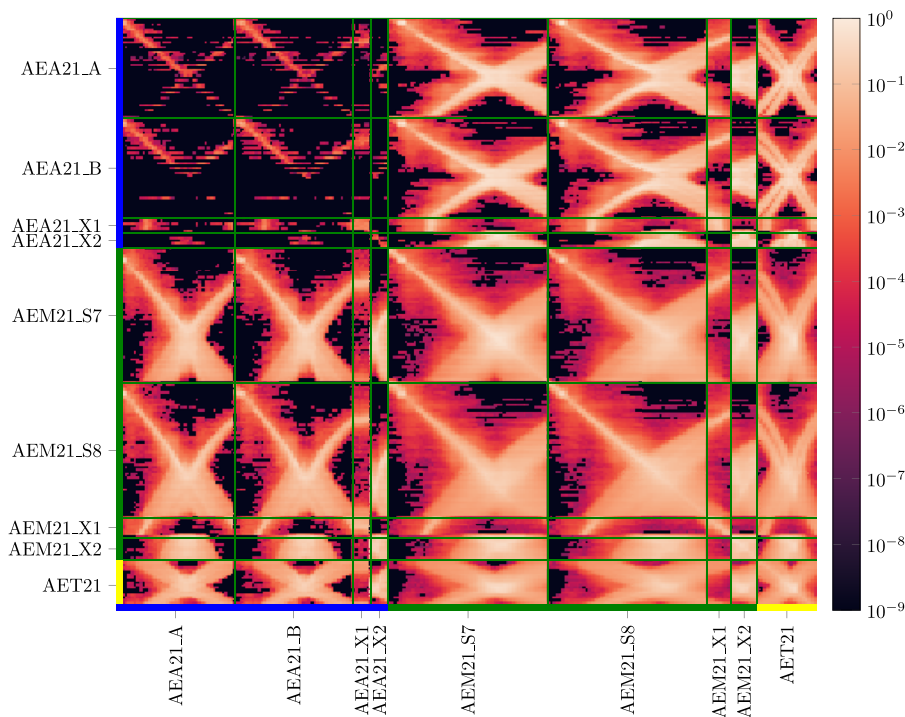


FIG. 8. Similar figure as 6, but the weight of a particle is calculated as the product of the blueshifted weights in the starting sightline times the redshifted weights in the detection sightline [first two terms of $s_{j,l}$ and last two terms of $s_{k,l}$ in Eq. (11)]. The maximum observed weight is 19 689.

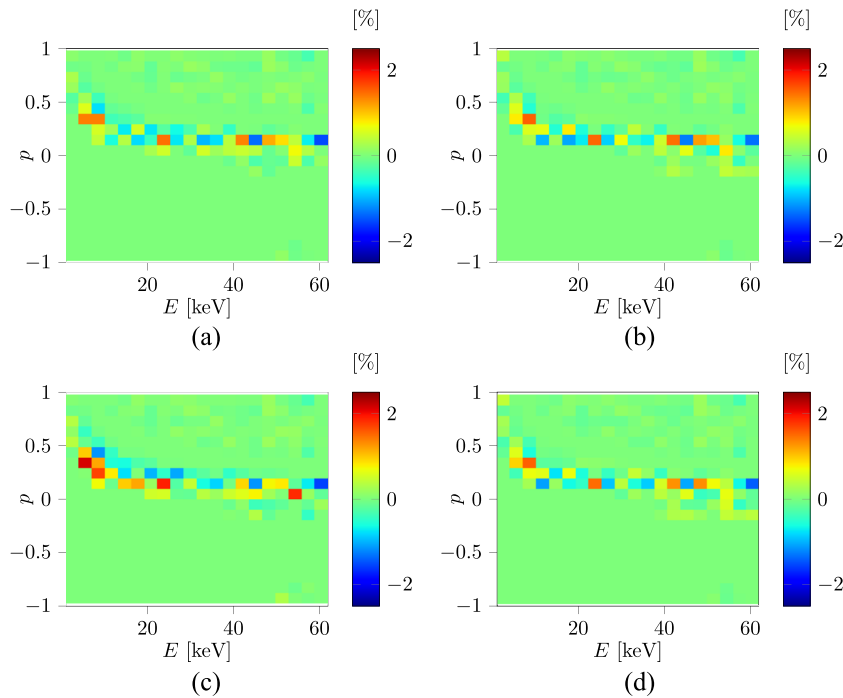


FIG. 9. Volume correlation between V_1 and V_2 for the (a) low iota (DBM), (b) high iota (FTM), (c) low mirror (AIM), and (d) high mirror (KJM) magnetic configurations. The color indicates the percentage difference between the distribution functions detected in V_2 , started in V_1 , for the given magnetic configuration, compared to the standard configuration (EIM).

Note that our analysis is not restricted to FIDA measurements alone. To do a similar analysis for other diagnostics, we can replace the weight functions used here with those of the particular diagnostic. Weight functions are available for neutral particle analyzers,³² neutron emission spectrometry,^{43,44} gamma-ray spectrometry,^{45,46} MeV proton diagnostics,⁴⁷ and fast-ion loss detectors.³⁰

V. CONCLUSION

The general correlation of fast ions between two arbitrary volumes for Wendelstein 7-X is investigated using BEAMS3D, a guiding-center code. It is observed that, for the investigated spatial regions, particular regions of velocity space are connected. Furthermore, it is observed that for these two volumes, the correlations in the velocity-space regions stay similar when changing the magnetic configuration. This could be explained by the volumes having identical magnetic configuration, due to the five-fold toroidal symmetry of the magnetic configuration of the stellarator.

The FIDA measurement system is investigated, and it is seen that there are three FIDA fans along the injection path for the two NBIs. The measurement volumes are approximately at the same toroidal position, and, thus, particles will return to roughly the same spatial locations and have a similar energy and pitch at each orbit due to conservation of energy and magnetic moment. Therefore, the correlation, for particles detected in two different sightlines, depends on whether they lie close to the same flux surface. When taking into account that the measurement in a sightline depends on the weight function, a relatively stronger correlation between sightlines on flux surfaces far apart is observed, since the weight functions select energetic particles that have larger drift velocities and, thus, have larger drift excursions across flux surfaces. A splitting of the spectrum into blueshifted and redshifted is done, and the correlation between the

blueshifted signal in the starting sightline and redshifted signal in the detection sightline is investigated. Due to the different angle with the magnetic field for the toroidal and oblique fans, a relatively larger cross correlation between the oblique and toroidal fans is observed compared to the internal fan correlation. Furthermore, since the oblique fans are able to detect particles with small pitch, a relatively larger internal oblique fan correlation is observed compared to that of the toroidal fan.

Similar theory can be used for investigating the correlation in gamma-ray spectroscopy, neutron emission spectroscopy, and Collective Thomson Scattering (CTS) measurements.

ACKNOWLEDGMENTS

This work has been carried out within the framework of the EUROfusion Consortium, funded by the European Union, via the Euratom Research and Training Program (Grant Agreement No. 101052200 - EUROfusion). The views and opinions expressed here are, however, those of the authors only and do not necessarily reflect those of the European Union or the European Commission. Neither the European Union nor the European Commission can be held responsible for them.

AUTHOR DECLARATIONS

Conflict of Interest

The authors have no conflicts to disclose.

Author Contributions

Jacob Emil Mencke: Conceptualization (equal); Formal analysis (lead); Investigation (lead); Methodology (lead); Software (equal);

Visualization (lead); Writing – original draft (lead); Writing – review & editing (equal). **Dmitry Moseev**: Conceptualization (equal); Methodology (equal); Supervision (equal); Writing – review & editing (supporting). **Mirko Salewski**: Conceptualization (equal); Supervision (equal); Writing – review & editing (equal). **Mads Rud Larsen**: Formal analysis (supporting); Investigation (supporting); Supervision (supporting); Writing – review & editing (supporting). **Bo Simmendefeldt Schmidt**: Supervision (supporting); Writing – review & editing (supporting). **Henrik Järleblad**: Conceptualization (supporting); Formal analysis (supporting); Supervision (supporting). **Samuel Lazerson**: Investigation (supporting); Software (equal); Writing – review & editing (supporting). **Peter Zsolt Poloskei**: Data curation (supporting). **Oliver Ford**: Data curation (supporting).

DATA AVAILABILITY

The data is available from the corresponding author upon reasonable request.

REFERENCES

- W. W. Heidbrink, “Fast-ion $D\alpha$ measurements of the fast-ion distribution,” *Rev. Sci. Instrum.* **81**, 10D727 (2010).
- L. Stagner, W. W. Heidbrink, M. Salewski, A. S. Jacobsen, B. Geiger, the DIII-D, ASDEX Upgrade Teams *et al.*, “Orbit tomography of energetic particle distribution functions,” *Nucl. Fusion* **62**, 026033 (2022).
- A. Fasoli, C. Gormenzano, H. Berk, B. Breizman, S. Briguglio, D. Darrow, N. Gorelenkov, W. Heidbrink, A. Jaun, S. Konovalov *et al.*, “Physics of energetic ions,” *Nucl. Fusion* **47**, S264 (2007).
- B. Simmendefeldt *et al.*, “4d and 5d phase-space tomography using slowing-down regularization and neural networks,” (unpublished).
- M. Salewski, B. Geiger, A. S. Jacobsen, M. García-Muñoz, W. Heidbrink, S. B. Korsholm, F. Leipold, J. Madsen, D. Moseev, S. K. Nielsen *et al.*, “Measurement of a 2D fast-ion velocity distribution function by tomographic inversion of fast-ion D-alpha spectra,” *Nucl. Fusion* **54**, 023005 (2014).
- M. Salewski, B. Geiger, A. Jacobsen, P. C. Hansen, W. Heidbrink, S. B. Korsholm, F. Leipold, J. Madsen, D. Moseev, S. K. Nielsen *et al.*, “High-definition velocity-space tomography of fast-ion dynamics,” *Nucl. Fusion* **56**, 106024 (2016).
- M. Weiland, B. Geiger, A. S. Jacobsen, M. Reich, M. Salewski, T. Odstrčil *et al.*, “Enhancement of the FIDA diagnostic at ASDEX upgrade for velocity space tomography,” *Plasma Phys. Controlled Fusion* **58**, 025012 (2016).
- M. Salewski, M. Nocente, A. Jacobsen, F. Binda, C. Cazzaniga, G. Ericsson, J. Eriksson, G. Gorini, C. Hellesen, A. Hjalmarsson *et al.*, “MeV-range velocity-space tomography from gamma-ray and neutron emission spectrometry at JET,” *Nucl. Fusion* **57**, 056001 (2017).
- M. Weiland, R. Bilato, B. Geiger, P. A. Schneider, G. Tardini, M. Garcia-Muñoz, F. Ryter, M. Salewski, H. Zohm *et al.*, “Phase-space resolved measurement of 2nd harmonic ion cyclotron heating using FIDA tomography at the ASDEX upgrade tokamak,” *Nucl. Fusion* **57**, 116058 (2017).
- B. Madsen, M. Salewski, J. Huang, A. S. Jacobsen, O. Jones, K. G. McClements, and M. Team, “Velocity-space tomography using prior information at mast,” *Rev. Sci. Instrum.* **89**, 10D125 (2018).
- B. Madsen, M. Salewski, W. W. Heidbrink, L. Stagner, M. Podestà, D. Lin, A. V. Garcia, P. C. Hansen, J. Huang *et al.*, “Tomography of the positive-pitch fast-ion velocity distribution in DIII-D plasmas with Alfvén eigenmodes and neoclassical tearing modes,” *Nucl. Fusion* **60**, 066024 (2020).
- B. Madsen, J. Huang, M. Salewski, H. Järleblad, P. Hansen, L. Stagner, J. Su, J. Chang, J. Fu, J. Wang *et al.*, “Fast-ion velocity-space tomography using slowing-down regularization in east plasmas with co-and counter-current neutral beam injection,” *Plasma Phys. Controlled Fusion* **62**, 115019 (2020).
- D. Moseev, M. Salewski, M. Garcia-Muñoz, B. Geiger, and M. Nocente, “Recent progress in fast-ion diagnostics for magnetically confined plasmas,” *Rev. Mod. Plasma Phys.* **2**, 7 (2018).
- D. Moseev and M. Salewski, “Bi-Maxwellian, slowing-down, and ring velocity distributions of fast ions in magnetized plasmas,” *Phys. Plasmas* **26**, 020901 (2019).
- J. D. Gaffey, “Energetic ion distribution resulting from neutral beam injection in tokamaks,” *J. Plasma Phys.* **16**, 149–169 (1976).
- S. Mazzi, J. Garcia, D. Zarzoso, Y. O. Kazakov, J. Ongena, M. Dreval, M. Nocente, Ž. Štancar, G. Szepesi, J. Eriksson *et al.*, “Enhanced performance in fusion plasmas through turbulence suppression by megaelectronvolt ions,” *Nat. Phys.* **18**, 776–782 (2022).
- M. Salewski, “Fast-ion diagnostic in fusion plasmas by velocity-space tomography,” Ph. D. thesis (Technical University of Denmark, 2019).
- O. Ford, L. Vanó, J. Alonso, J. Baldzuhn, M. Beurskens, C. Biedermann, S. Bozhenkov, G. Fuchert, B. Geiger, D. Hartmann *et al.*, “Charge exchange recombination spectroscopy at Wendelstein 7-X,” *Rev. Sci. Instrum.* **91**, 023507 (2020).
- M. Salewski, B. Geiger, D. Moseev, W. Heidbrink, A. S. Jacobsen, S. B. Korsholm, F. Leipold, J. Madsen, S. K. Nielsen, J. Rasmussen *et al.*, “On velocity-space sensitivity of fast-ion D-alpha spectroscopy,” *Plasma Phys. Controlled Fusion* **56**, 105005 (2014).
- R. Jaspers, M. Scheffer, A. Kappatou, N. van der Valk, M. Durkut, B. Snijders, O. Marchuk, W. Biel, G. Pokol, G. Erdei *et al.*, “A high etendue spectrometer suitable for core charge eXchange recombination spectroscopy on ITER,” *Rev. Sci. Instrum.* **83**, 10D515 (2012).
- M. Salewski, S. K. Nielsen, H. Bindslev, V. Furtula, N. Gorelenkov, S. B. Korsholm, F. Leipold, F. Meo, P. Michelsen, D. Moseev *et al.*, “On velocity space interrogation regions of fast-ion collective Thomson scattering at ITER,” *Nucl. Fusion* **51**, 083014 (2011).
- M. Salewski, F. Meo, M. Stejner, O. Asunta, H. Bindslev, V. Furtula, S. B. Korsholm, T. Kurki-Suonio, F. Leipold, F. Leuterer *et al.*, “Comparison of fast ion collective Thomson scattering measurements at ASDEX Upgrade with numerical simulations,” *Nucl. Fusion* **50**, 035012 (2010).
- M. Nishiura, S. Kubo, K. Tanaka, R. Seki, S. Ogasawara, T. Shimozuma, K. Okada, S. Kobayashi, T. Mutoh, K. Kawahata *et al.*, “Spectrum response and analysis of 77 GHz band collective Thomson scattering diagnostic for bulk and fast ions in LHD plasmas,” *Nucl. Fusion* **54**, 023006 (2014).
- D. Moseev, H. P. Laqua, T. Stange, I. Abramovic, S. K. Nielsen, S. Äkäslompolo, K. Avramidis, H. Braune, G. Gantenbein, S. Illy *et al.*, “Collective Thomson scattering diagnostic for Wendelstein 7-X at 175 GHz,” *J. Instrum.* **15**, C05035 (2020).
- M. Nocente, Y. O. Kazakov, J. Garcia, V. Kiptily, J. Ongena, M. Dreval, M. Fitzgerald, S. E. Sharapov, Z. Štancar, H. Weisen *et al.*, “Generation and observation of fast deuterium ions and fusion-born alpha particles in JET D-³He plasmas with the 3-ion radio-frequency heating scenario,” *Nucl. Fusion* **60**, 124006 (2020).
- V. G. Kiptily, F. E. Cecil, and S. S. Medley, “Gamma ray diagnostics of high temperature magnetically confined fusion plasmas,” *Plasma Phys. Controlled Fusion* **48**, R59 (2006).
- M. Nocente, M. Tardocchi, R. Barnsley, L. Bertalot, B. Brichard, G. Croci, G. Brolatti, L. Di Pace, A. Fernandes, L. Giacomelli *et al.*, “Conceptual design of the radial gamma ray spectrometers system for α particle and runaway electron measurements at ITER,” *Nucl. Fusion* **57**, 076016 (2017).
- W. W. Heidbrink, K. H. Burrell, Y. Luo, N. A. Pablant, and E. Ruskov, “Hydrogenic fast-ion diagnostic using Balmer-alpha light,” *Plasma Phys. Controlled Fusion* **46**, 1855 (2004).
- S. Äkäslompolo, P. Drewelow, Y. Gao, A. Ali, C. Biedermann, S. Bozhenkov, C. P. Dhard, M. Endler, J. Fellingner, O. P. Ford, B. Geiger, J. Geiger, N. d. Harder, D. Hartmann, D. Hathiramani, M. Isobe, M. Jakubowski, Y. Kazakov, C. Killer, S. Lazerson, M. Mayer, P. McNeely, D. Naujoks, T. W. C. Neelis, J. Kontula, T. Kurki-Suonio, H. Niemann, K. Ogawa, F. Pisano, P. Z. Poloskei, A. P. Sitjes, K. Rahbarnia, N. Rust, J. C. Schmitt, M. Slecza, L. Vano, A. v. Vuuren, G. Wurden, and R. C. Wolf, “Validating the ASCOT modelling of NBI fast ions in Wendelstein 7-X stellarator,” *J. Instrum.* **14**, C10012 (2019).
- J. Galdon-Quiroga, M. Garcia-Munoz, K. McClements, M. Nocente, S. Denk, S. Freethy, A. Jacobsen, F. Orain, J. Rivero-Rodriguez, M. Salewski *et al.*,

- “Observation of accelerated beam ion population during edge localized modes in the ASDEX Upgrade tokamak,” *Nucl. Fusion* **59**, 066016 (2019).
- ³¹B. Geiger, A. N. Karpushov, B. P. Duval, C. Marini, O. Sauter, Y. Andrebe, D. Testa, M. Maraschek, M. Salewski, P. A. Schneider *et al.*, “Fast-ion transport in low density L-mode plasmas at TCV using FIDA spectroscopy and the TRANSP code,” *Plasma Phys. Controlled Fusion* **59**, 115002 (2017).
- ³²W. W. Heidbrink, Y. Luo, K. H. Burrell, R. W. Harvey, R. I. Pinsker, and E. Ruskov, “Measurements of fast-ion acceleration at cyclotron harmonics using Balmer-alpha spectroscopy,” *Plasma Phys. Controlled Fusion* **49**, 1457 (2007).
- ³³M. Osakabe, S. Murakami, M. Yoshinuma, K. Ida, A. Whiteford, M. Goto, D. Kato, T. Kato, K. Nagaoka, T. Tokuzawa *et al.*, “Fast ion charge exchange spectroscopy measurement using a radially injected neutral beam on the large helical device,” *Rev. Sci. Instrum.* **79**, 10E519 (2008).
- ³⁴M. Podestà, W. W. Heidbrink, R. E. Bell, and R. Feder, “The NSTX fast-ion D-alpha diagnostic,” *Rev. Sci. Instrum.* **79**, 10E521 (2008).
- ³⁵Y. Hou, C. Wu, J. Huang, W. Heidbrink, M. von Hellermann, Z. Xu, Z. Jin, J. Chang, Y. Zhu, W. Gao *et al.*, “Fast-ion D_α spectrum diagnostic in the EAST,” *Rev. Sci. Instrum.* **87**, 11E552 (2016).
- ³⁶S. Jianxun, W. Baonian, J. Huang, B. Madsen, M. Salewski, S. Yanxu, W. Jinfang, F. Jing, J. Chang, W. Chengrui *et al.*, “Reconstructions of velocity distributions from fast-ion D-alpha (FIDA) measurements on EAST,” *Plasma Sci. Technol.* **23**, 095103 (2021).
- ³⁷J. Huang, J. P. Qian, A. M. Garofalo, X. Z. Gong, C. R. Wu, J. F. Chang, J. Zhang, H. F. Du, M. Q. Wu, B. L. Hao, L. M. Yu, X. M. Zhang, B. Madsen, M. Salewski, L. Z. Liang, J. Li, S. Y. Ding, G. Q. Zhong, J. L. Chen, X. Zhu, L. Zeng, E. Z. Li, B. Zhang, Z. Xu, J. X. Su, W. Gao, Y. J. Chen, Y. Y. Li, H. Liu, B. Lyu, Q. Zang, B. Wan, the EAST Team, “Improved high-performance fully non-inductive discharge by optimizing the fast-ion confinement on EAST,” *Nucl. Fusion* **60**, 016002 (2019).
- ³⁸B. Geiger, M. Weiland, A. S. Jacobsen, D. Rittich, R. Dux, R. Fischer, C. Hopf, M. Maraschek, R. McDermott, S. K. Nielsen *et al.* “Fast-ion transport and neutral beam current drive in ASDEX upgrade,” *Nucl. Fusion* **55**, 083001 (2015).
- ³⁹W. W. Heidbrink, D. Liu, Y. Luo, E. Ruskov, and B. Geiger, “A code that simulates fast-ion D_α and neutral particle measurements,” *Commun. Comput. Phys.* **10**, 716–741 (2011).
- ⁴⁰M. McMillan and S. A. Lazerson, “BEAMS3D neutral beam injection model,” *Plasma Phys. Controlled Fusion* **56**, 095019 (2014).
- ⁴¹S. A. Lazerson, O. P. Ford, C. Nuehrenberg, S. Äkäslompolo, P. Z. Poloskei, M. Machielsens, P. McNeely, L. Vanó, N. Rust, S. Bozhenkov, T. W. C. Neelis, J. P. Graves, D. Pfefferlé, A. Spanier, D. Hartmann, N. Marushchenko, Y. Turkin, M. Hirsch, N. Chaudhary, U. Hoefel, T. Stange, G. Weir, N. Pablant, A. Langenberg, P. Traverso, P. Valson, J. Knauer, K. Jakob Brunner, E. Pasch, M. Beurskens, H. Damm, G. Fuchert, P. Nelde, E. Scott, U. Hergenbald, A. Pavone, K. Rahbarnia, T. Andreeva, J. Schilling, C. Brandt, U. Neuner, H. Thomsen, M. Jakubowski, A. Ali, Y. Gao, H. Niemann, A. Puig Sitjes, R. Koenig, R. C. Wolf, the W7-X Team, “Validation of the BEAMS3D neutral beam deposition model on Wendelstein 7-x,” *Nucl. Fusion* **60**, 076020 (2020).
- ⁴²P. Helander, “Theory of plasma confinement in non-axisymmetric magnetic fields,” *Rep. Prog. Phys.* **77**, 087001 (2014).
- ⁴³A. Jacobsen, F. Binda, C. Cazzaniga, J. Eriksson, A. Hjalmarsson, M. Nocente, M. Salewski, G. Tardini, JET Contributors, ASDEX Upgrade Team, “Velocity-space sensitivities of neutron emission spectrometers at the tokamaks JET and ASDEX Upgrade in deuterium plasmas,” *Rev. Sci. Instrum.* **88**, 073506 (2017).
- ⁴⁴A. S. Jacobsen, M. Salewski, J. Eriksson, G. Ericsson, S. B. Korsholm, F. Leipold, S. K. Nielsen, J. Rasmussen, M. Stejner, JET EFDA Contributors, “Velocity-space sensitivity of neutron spectrometry measurements,” *Nucl. Fusion* **55**, 053013 (2015).
- ⁴⁵M. Salewski, M. Nocente, G. Gorini, A. S. Jacobsen, V. Kiptily, S. B. Korsholm, F. Leipold, J. Madsen, D. Moseev, S. K. Nielsen *et al.*, “Velocity-space observation regions of high-resolution two-step reaction gamma-ray spectroscopy,” *Nucl. Fusion* **55**, 093029 (2015).
- ⁴⁶M. Salewski, M. Nocente, G. Gorini, A. S. Jacobsen, V. Kiptily, S. B. Korsholm, F. Leipold, J. Madsen, D. Moseev, S. K. Nielsen *et al.*, “Fast-ion energy resolution by one-step reaction gamma-ray spectrometry,” *Nucl. Fusion* **56**, 046009 (2016).
- ⁴⁷W. Heidbrink, A. Garcia, W. Boeglin, and M. Salewski, “Phase-space sensitivity (weight functions) of 3 MeV proton diagnostics,” *Plasma Phys. Controlled Fusion* **63**, 055008 (2021).